Available online at www.sciencedirect.com
SCIENCE DIRECT®
International Journal of Heat and Mass Transfer 48 (2005) 1252–1266
International Journal of HEAT and MASS TRANSFER
www.elsevier.com/locate/ijhmt

Convective heat transfer from a partially premixed impinging flame jet. Part II: Time-resolved results

S.G. Tuttle [1], B.W. Webb *, M.Q. McQuay [2]

Department of Mechanical Engineering, Brigham Young University, 435 CTB, Provo, UT 84602, United States

Received 5 April 2004; received in revised form 11 October 2004
Available online 19 December 2004

Abstract

This is the second of a two-part paper on heat transfer from an impinging flame jet reporting time-resolved results. Axial and radial profiles of time-resolved local heat fluxes of methane–air jet flames impinging normal to a cooled plate are reported, including the root mean square (RMS), probability distribution function (PDF), and the power spectral density (PSD) of the heat flux fluctuations as a function of equivalence ratio, Reynolds number, and nozzle-plate spacing. The RMS, PDF, and PSD of the heat flux signal from the stagnation point and along the plate revealed correlation of the local heat flux to the flame structure. Impingement heat flux from premixed nozzle-stabilized flames was characterized by small RMS fluctuations and frequency behavior indicating the formation of weak, buoyancy-driven vortex structures at the shear layer between the hot gases surrounding the flame and the ambient air. Conversely, diffusion flames were characterized by much larger RMS fluctuations and PSD's indicating the development of much larger vortex structures. Time-resolved heat flux for lifted flames varied according to flame structure and combustion intensity. PSD magnitudes were related to the range of temperatures in the flow; greater temperature ranges produced larger heat flux variations. The contributing frequencies were related to the duration of the heat flux fluctuation; more rapid changes in heat flux produced higher frequency content.

1. Introduction

A summary of experimental work focusing on heat transfer characteristics of impinging flame jets was presented in Part I of this work. Part I documented visually observed flame structure for partially premixed flames impinging on a cooled plate. The dependence of local, time-mean heat flux along the impingement plate on nozzle Reynolds number, nozzle-plate spacing, and equivalence ratio was presented. Little is known about the fluctuations in local heat flux for such impinging flame jets, although there is substantial time-mean information collected for various flow conditions and fuels. This may be due to inadequate instrumentation available in prior studies, with poor spatial and/or temporal resolution [1]. Developments in thermopile construction have produced small sensors that can respond to rapid fluctuations in heat flux. This allows observation of the fluctuating heat flux in laminar, transitional, and turbulent flames and the prevalent frequency behavior that dominate these flow structures in the shear layers of

* Corresponding author. Tel.: +1 801 422 6543; fax: +1 801 422 0516.
E-mail address: webb@byu.edu (B.W. Webb).
[1] Present address: Pratt & Whitney, Hartford, CT.
[2] Present address: Oblon, Spivak, McClelland, Maier, & Neustadt P.C., 1940 Duke Street, Alexandria, VA 22314.

0017-9310/$ - see front matter © 2004 Elsevier Ltd. All rights reserved.
doi:10.1016/j.ijheatmasstransfer.2004.10.028

Nomenclature

d	nozzle diameter
h	nozzle-plate spacing
H	dimensionless nozzle-plate spacing, h/d
q''	local heat flux
r	radial distance from stagnation point
R	dimensionless radial distance from stagnation point, r/d
Re	nozzle Reynolds number, based on nozzle diameter and physical properties of the unburned methane–air mixture at the nozzle exit, $\rho V d/\mu$
V	average fluid velocity at nozzle exit
f_s	sampling frequency

Greek symbols

Φ	equivalence ratio, the ratio of the stoichiometric to actual air-to-fuel ratio, $\Phi = (A/F)_{stoich}/(A/F)_{act}$
μ	gas mixture dynamic viscosity
ρ	gas mixture density

flames [2–4]. Baukal and Gebhart noted the lack of suitable instrumentation in early studies [1]. The steady-state measurement methods are insufficient to observe the rapid fluctuations of the heat flux at the plate face that occur in turbulent flow.

Studies have been conducted to observe the influence of turbulent flame behavior on heat transfer and flame structures. The rapid mixing found in turbulent flows increases the heat and mass diffusion and the resulting rate of combustion and wall heat flux. In order to understand and characterize the influence of turbulence on heat flux and the flame structure, a number of studies have been conducted (see, for example, [5–12]). Temperature and velocity oscillations in flames have also been explored experimentally. Oscillation frequencies have been found to be a function of Reynolds number, equivalence ratio, and the dimensionless nozzle-plate spacing H [2,3,13–15].

Part I of this work summarized investigations focusing on the time-mean heat transfer characteristics of impinging flame jets. To the authors' knowledge, there are no prior studies that document the corresponding time-resolved heat transfer behavior. This second part of a two-part study seeks to fill this void in understanding by exploring the time-resolved characteristics of impinging, partially premixed impinging flame jets for a range of Reynolds number, equivalence ratio, nozzle-plate spacing, and radial location along the impingement plate. It is again stated here that although the heat/mass transfer phenomena for this problem are a complex interplay of flow structure, diffusion of species and energy, chemical reaction and associated heat release, etc., the focus here is on heat transfer to the impingement plate. Where appropriate, the time-resolved behavior is correlated with the time-average characteristics observed in Part I of the study.

2. Experimental method

Significant details about the experimental method, procedure, uncertainty, and conditions have already been presented in Part I. Attention is focused here on the details of the time-resolved measurements. The instrumentation and subsequent data processing were carried out on a PC-based system. A total of 2^{18} data points were collected in a contiguous temporal data set for each experimental condition and measurement location. The number of measurements used in determining the fluctuation statistics was determined by sequentially increasing the number of data points in a set to calculate the statistics until the mean and RMS flux ceased to change by more than two percent. Preliminary sampling was also performed for a given experimental condition over a range of sampling frequencies from f_s = 10–30 kHz to determine the appropriate data acquisition rate and the approximate frequency content of the fluctuating heat flux signal. The mean value and the RMS were found to be independent of the sampling frequency in this range. Therefore, the sampling frequency was determined such that the Nyquist frequency, f_N ($=0.5f_s$), would be greater than any significant anticipated signals, as observed in preliminary studies. Thus, any signal must decay to the noise floor at a frequency less than f_N. The noise floor was characterized by recording data without imposed heat flux or temperature input. Several contiguous data sets were collected at various sampling frequencies (as high as 30 kHz) at the same experimental conditions and measurement location (Re = 5500, Φ = 6.7, R = 6, and H = 20). This radial location was selected because it exhibited the largest RMS at this fuel flow rate, mixture stoichiometry, and nozzle-plate spacing. It was discovered that the magnitude of the component frequencies fell to that of the baseline noise at approximately 1–2 kHz, and remained at the noise floor out to 30 kHz. Therefore, the sampling frequency was chosen to be 10 kHz, allowing any significant behavior in the frequency domain to be represented accurately up to the Nyquist frequency, 5 kHz. All time-resolved data were thus collected at 10 kHz and stored for later retrieval and analysis.

The post-processing procedure converted the stored voltages from their binary format to double precision ASCII format. These voltages were used to calculate the instantaneous temperatures and heat fluxes using the calibration provided by the manufacturer. The mean, standard deviation, skewness, and kurtosis were then calculated for the heat flux. Further, in order to calculate the frequency content of the time-resolved heat flux fluctuations, the contiguous data sets of 2^{18} data points were first divided into 32 blocks of 2^{13} elements and filtered by a Hanning window. The power spectral density function (PSD), a measure of the power in the fluctuating heat flux signal at each frequency, was calculated for each block with a frequency resolution of 1.22 Hz. This was done by performing a fast Fourier transform of the signal to determine the component frequencies and respective amplitudes. The PSD magnitudes were calculated using established methods [16]. The magnitudes at the frequencies of each block were then averaged. The number of blocks employed was selected as a compromise between maximum frequency resolution and minimum noise in the PSD. Each time an experiment was run, a data set was gathered without a flame to provide a noise-floor PSD for that condition. All of the noise-floor PSD's were averaged to determine a mean noise floor. High frequencies were filtered from the PSD's with a signal-to-noise ratio cut-off of 2. The probability density function (PDF), reflective of the magnitude the fluctuating heat flux may assume with its respective probability, was also determined [17]. The difference between measured minimum and maximum heat flux was divided into 500 increments in the calculation of the PDF. The experimental method and data reduction for the time-resolved measurements are explained in greater detail elsewhere [18].

3. Results and discussion

The time-resolved heat flux data, comprising the RMS, PSD, and PDF, will be presented in this section. The qualitative flame structure and corresponding time-mean local wall heat flux, with their dependence on the parameters varied in this study were reported in Part I.

The RMS, PSD, and the PDF of a particular heat flux signal may be correlated to the local thermal structure of the gases. The RMS indicates the variation of the fluctuations about the mean in the heat flux signal. The PSD plots the frequencies and the respective intensity at each that make up the fluctuations in the heat flux signal. Rapid fluctuations, indicated by larger frequencies in the PSD, suggest small structures rapidly changing the temperature gradient in the local boundary layer at the impingement plate. The PSD magnitudes, graphed as a function of frequency, indicate the heat flux variance that occurs at a particular frequency. Thus, the area under a PSD curve represents the RMS. In this study, the PDF of a heat flux signal reflects the fraction of time the sensor was exposed to a particular heat flux, revealing the prominent heat fluxes and indicating their statistical distribution. The skewness coefficient, which reflects the asymmetry of PDF relative to a normal distribution, was also calculated.

The discussion of time-resolved heat flux behavior will follow the same sequence used in Part I of this study. The characteristics of nozzle-stabilized flames will first be discussed, followed by the behavior of lifted flames. Although somewhat awkward, the exploration of time-resolved behavior presented here will necessarily refer to the documented flame structure and mean heat flux discussion of Part I.

3.1. Nozzle-stabilized flame

The local mean, RMS, PSD, and PDF heat flux profiles, measured radially from the stagnation point of a nozzle-stabilized flame at $Re = 1500$, $\Phi = 4$, and $H = 15$, are shown in Fig. 1a–c, respectively. A photograph of the flame for this experimental condition is shown in Fig. 4a of Part I. In Fig. 1a the vertical dashed line represents the radial location where the visible tip of the flame was observed. The RMS heat flux in Fig. 1a reveals a gradual increase in the heat flux RMS with distance from the stagnation point out to $R = 5$, followed by a gradual decrease and a slight inflection at the flame tip ($R \approx 10$). From the discussion of the flame structure in Part I it may be observed that the distance between the flame surface and the plate begins to increase at the same radial location as the RMS peak ($R = 5$). This indicates that the temperature in the hot products were increasing, suggesting that the heating and expansion of the gases cause the flame surface to separate from the plate. The subsequent decrease in the RMS and mean with distance from the stagnation point may be interpreted as a result of the narrowing in the temperature range in the boundary layer as the cool unburned gases were heated by the combustion products.

The PSD (Fig. 1b) at the stagnation point ($R = 0$) reveals two preferred frequencies: a harmonic frequency at 12 Hz and its sub-harmonic at 24 Hz. The frequency peaks are a result of the vortices formed by the buoyancy-driven shear layer that lie at the interface between the hot gases surrounding the flame and ambient air in the pre-impingement jet. As the vortex rotates and translates along the free jet and the wall jet, it causes the flame to bulge and contract. The primary harmonic suggests that the bulging and contraction in the flame structure causes the temperature in the boundary layer to oscillate as the gases flow past the impingement plate. A study of Yule [19] documented the formation and behavior of vortices in the outer mixing layer of a non-reacting

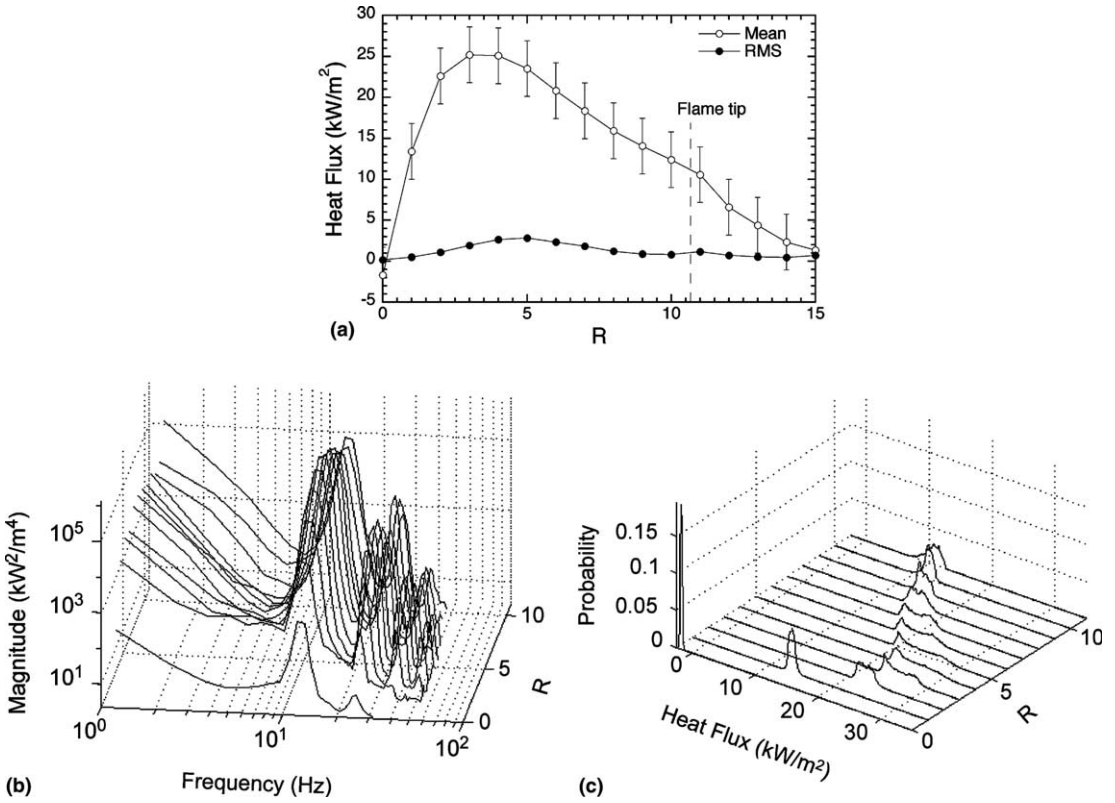

Fig. 1. Heat flux radial variations of (a) mean and RMS; (b) PSD's; and (c) PDF's for a flame with $Re = 1500$, $\Phi = 4.0$, and $H = 15$.

round jet. These vortices, formed at the interface of the hot products and ambient air, have also been documented and studied for free flame jets [15,20–24]. It has been confirmed that a buoyancy-driven shear layer between the hot gases and the ambient air produces outer structures with characteristic frequencies between 5 and 20 Hz. These structures develop in size with increasing axial distance from the nozzle exit. The sub-harmonic at 24 Hz suggests that as the vortices develop with axial distance from the nozzle exit, a fold in the layers of hot and cool gases is formed. This produces another fluctuation in the heat flux at twice the frequency of the harmonic. Downstream of the stagnation zone, the number of frequency peaks in Fig. 1b increases to four, indicating that as the vortices impinge against the plate, more folds in the layer of hot and cool gases are produced, with preferred frequencies appearing in the PSD at multiples of the harmonic frequency.

The magnitude of the preferred frequency peaks increases, then decreases with distance from the stagnation point, with a maximum approximately five diameters from the stagnation point. Recall from the discussion on flame structure in Part I that, at a radial location four diameters from the stagnation point, the flame is nearest the plate. Immediately downstream, the flame begins to separate from the plate with increasing distance from the stagnation zone. The radial location of the flame separation ($R = 5$) corresponds roughly to the location of maximum magnitude of the dominant frequency, or the location where the temperature fluctuations in the flow were the largest. Here, the heat flux fluctuations have the greatest magnitude as the wall jet flame surfaces, and the unburned gases and hot combustion products are mixed by the vortex structures. Beyond $R = 5$, the magnitudes of all of the frequency peaks diminish with distance from the stagnation zone, confirming that the separation of the flame from the plate and the reduction in both the heat release and wall jet velocity result in a decrease in the amplitude of the heat flux fluctuations. At the flame tip, at $R = 11$, visual flickering of the flame increases the magnitude of the heat flux fluctuations.

The PDF's in Fig. 1c reveal further insight into the flame behavior as it impinges against the plate. The PDF at the stagnation point is relatively narrow, and PDF's widen at locations farther from the stagnation point until $R = 5$, beyond which there is a gradual narrowing of the distributions. Additionally, the distributions exhibit two relatively weak peaks between two and eight diameters from the stagnation point. The bimodal distributions suggest that the impingement plate

was exposed to gases which alternated between two predominant temperature ranges, confirming the existence of vortices mixing hot products near the flame. Beyond eight diameters from the stagnation point, the PDF's exhibit a single peak. Again, the flickering at the flame tip resulted on an increase in the distribution range at $R = 11$.

Fig. 2 shows the variation in the RMS, PSD, and PDF radial heat flux profiles with changes in nozzle-plate spacing for nozzle-stabilized flames at an experimental condition $Re = 1500$ and $\Phi = 4$. The radial RMS heat flux profiles for flames at nozzle-plate spacings of 5, 15, and 25 diameters are shown in Fig. 2a (see flames in Fig. 4b, a, and c, respectively, in Part I). It is observed generally that the RMS heat flux increases with increasing nozzle-plate spacing. Indeed, fluctuations in wall flux are very low for $H = 5$, but exhibit a dramatic increase at the $H = 15$ and 25 experimental conditions. Interestingly, the RMS heat flux for the intermediate nozzle-plate spacing ($H = 15$) is generally the highest. It may be speculated that the nozzle-plate spacing $H = 15$ is a transition condition between the case of little heat/mass diffusion with corresponding reaction and heat release in the pre-impingement jet for $H = 5$, and significant, developed diffusion and reaction for the greater nozzle-plate spacing $H = 25$. The initial general increase in RMS heat flux with radial position for all three nozzle-plate spacings may be a result of two contributing factors. The first relates to the narrower separation between the wall jet flame and the plate, producing a general increase in the temperature oscillations with increasing distance from the stagnation point as the remaining unburned gases were consumed. The peak RMS heat flux occurs downstream of observed maxima in the time-mean local heat flux, seen in Part I, Fig. 7b. As the reaction ceases, fluctuations also cease resulting in decreases in RMS heat flux with radius. A second factor may be associated with the development of buoyancy-driven vortices in the longer pre-impingement jet for $H = 15$ and 25 (but which are non-existent for $H = 5$), which prevail in the early wall jet region.

Fig. 2b and c illustrate radial profiles of PSD's and PDF's, respectively, for the flame with $Re = 1500$, $\Phi = 4$, and $H = 5$, corresponding to the flame photograph of Fig. 4b in Part I. There is no indication of vortex-induced heat flux fluctuations, evidenced by the absence of preferred frequencies in the PSD of Fig. 2b. In comparison to the PDF's in Fig. 1c for $H = 15$, the probability density function for $H = 5$ in Fig. 2c reveals considerably narrower fluctuations in the heat flux about the mean, again indicating reduced oscillations in temperature gradient.

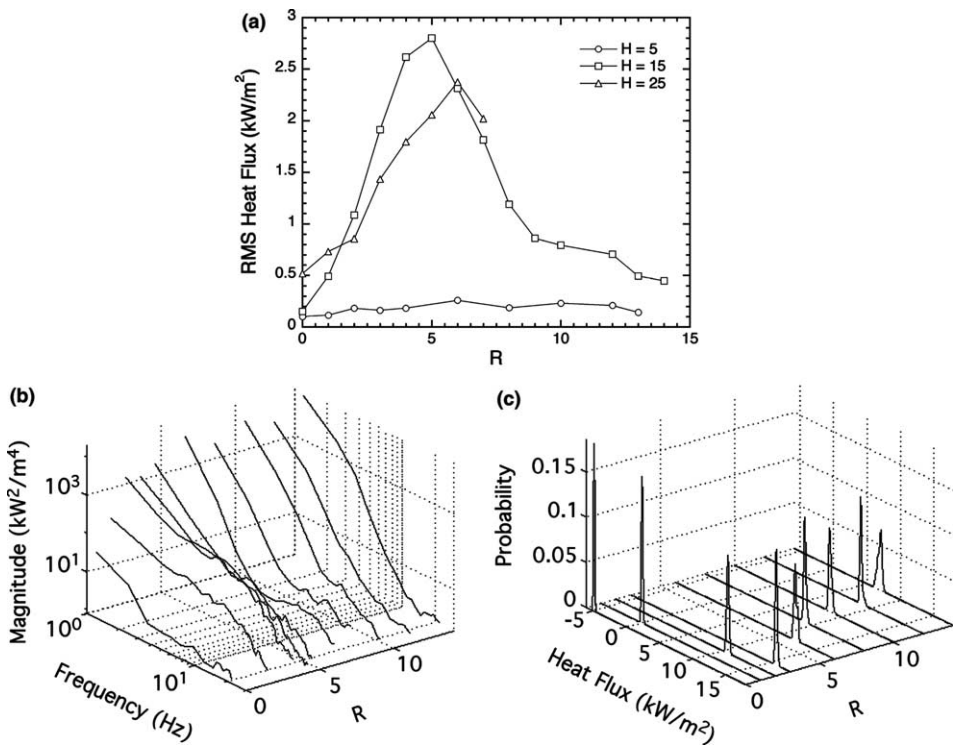

Fig. 2. Heat flux radial variations for a flame with $Re = 1500$, and $\Phi = 4.0$, illustrating (a) the effect of various nozzle-plate spacings on mean and RMS heat flux; (b) PSD's and (c) PDF's for $H = 5$.

The variation in time-resolved stagnation heat flux with equivalence ratio for nozzle-stabilized flames is shown in the RMS profile and the PSD profile of Fig. 3a and b, respectively, for a Reynolds number of 1500 and a nozzle-plate spacing of 15 diameters. The curve for the time-mean heat flux in Fig. 3a reflects the changes in the flame structure with increasing equivalence ratio. Recall from the discussion on flame structures from Part I that combustion in the premixed flame is nearly complete prior to impingement against the plate for $\Phi = 1.0$, resulting in the maximum heat flux at $\Phi = 1.0$ evident in Fig. 3a. As the inner cone of the premixed flame stretches upward and outward with increasing equivalence ratio, the stagnation heat flux decreases, until at $\Phi = 2.0$, the heat flux has decreased to 1.1 kW/m^2. At greater equivalence ratios, all of the time-mean stagnation heat fluxes are negative, characteristic of a cool, unreacted core in the free jet. The RMS profile in Fig. 3a shows a slight increase in heat flux fluctuation as the equivalence ratio increases from 1.0 to 1.5, as the premixed flame becomes richer and the inner flame cone stretches upward to the plate. The inner cone impinges against the plate for the flame with $\Phi = 1.5$, while that of the flame at $\Phi = 1.0$ burns short of the plate. Therefore, as the flame fluctuates, the temperature excursions in the gases near the plate are expected to be larger for the flame with $\Phi = 1.5$, varying between the temperature limits of the unburned gases and the hot combustion products. As the equivalence ratio is increased beyond 2, the flame transitions to diffusion-controlled combustion and the cool potential core impinges at the stagnation point, changing little with further increases in Φ.

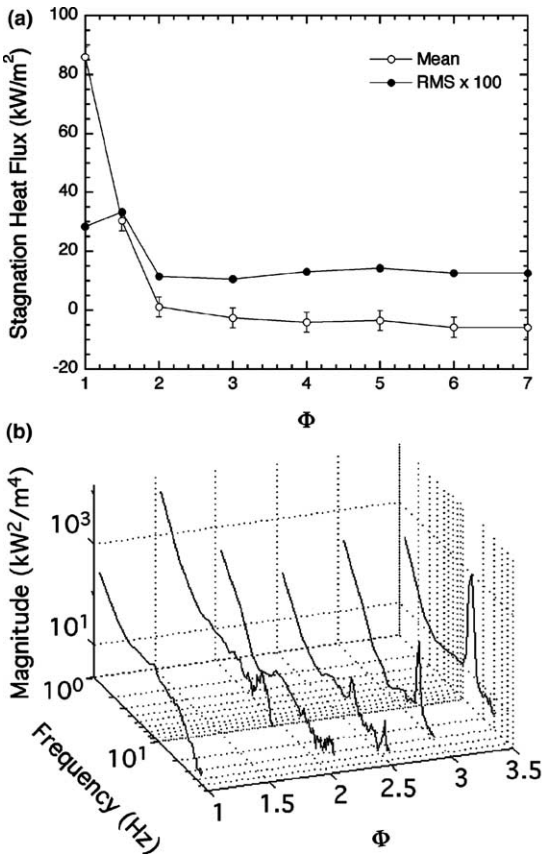

Fig. 3. The effect of equivalence ratio on (a) mean and RMS; and (b) PSD's of stagnation heat flux for a flame with $Re = 1500$ and $H = 15$.

The clearest trend in the heat flux PSD's of Fig. 3b is the appearance of preferred frequencies as the equivalence ratio increases and the flame transitions from premixed to diffusion-controlled combustion. A 12-Hz peak emerges at $\Phi = 2.5$ and grows in magnitude with increasing Φ. Visible flickering of the flame was only observed for equivalence ratios greater than two. For equivalence ratios greater than $\Phi = 2.5$, there is a significant increase in the strength of the harmonic. This may suggest that for $\Phi < 2.5$, buoyancy-driven vortices do not develop in the pre-impingement flame jet. As the equivalence ratio was increased beyond 3.5 (not shown), there were no significant changes in the time-resolved heat flux behavior. The decrease in the development of the buoyancy-driven vortex structures at low equivalence ratios may be attributed to the differences between premixed (localized) and diffusion-controlled (distributed) combustion. For premixed flames, the bulk of the heat release occurs within the free jet where the local velocity is equal to the laminar flame speed. Conversely, a diffusion flame with the same Reynolds number will yield a longer, distributed region of combustion surrounding the unburned free jet. This creates a region of hot, buoyant gases surrounding the flame and a long shear layer for vortex development.

Differences in radial profiles of time-resolved heat flux behavior with changes in equivalence ratio for nozzle-stabilized flames are shown in Fig. 4. Radial RMS heat flux measurements for flames with $Re = 1500$, $H = 15$, and $\Phi = 1.0$, 1.5, 4.0, and 7.0 are shown in Fig. 4a. The flames with $\Phi = 1.0$ and 1.5, described and shown in Part I Fig. 4d and c, exhibited premixed behavior, while the remaining two ($\Phi = 4.0$ and 7.0, Part I Fig. 4a and f, respectively) were diffusion-controlled. From these RMS profiles, characteristic differences in RMS heat flux between premixed and diffusion flames can be seen. Premixed flames ($\Phi = 1.0$ and 1.5) exhibit higher heat flux RMS fluctuations near the stagnation point than their diffusion flame counterparts ($\Phi = 4.0$ and 7.0). For these premixed flames the heat flux RMS rises to a maximum near $R = 1.5$, then decreases as the gas velocity decreases and the flame dwindles in the wall jet. Diffusion flames ($\Phi = 4.0$ and 7.0) exhibit a dramatic increase in RMS heat flux with radius, believed to be due

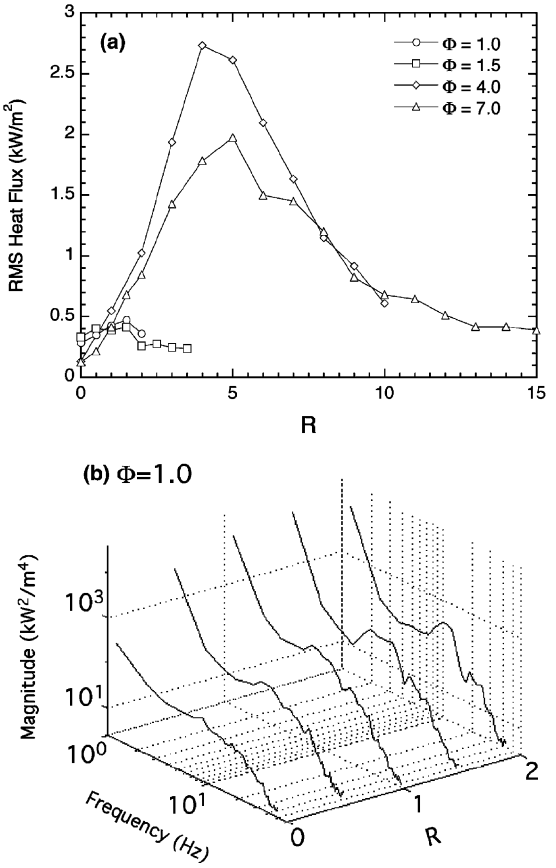

Fig. 4. For a flame with $Re = 1500$ and $H = 15$, (a) the effect of various equivalence ratios on radial RMS heat flux; and (b) radial PSD profile for $\Phi = 1.0$.

to the transport of hot gas and perhaps cool ambient air to the boundary layer by buoyancy-driven vortex motion.

The radial variation of PSD's for a flame with $Re = 1500$, $\Phi = 1.0$, and $H = 15$ is illustrated in Fig. 4b. A broad preferred frequency peak centered near 10 Hz emerges at a radial location $R = 0.5$ and begins to grow with increasing radial distance from the stagnation point. This suggests the formation of buoyancy- and/or shear-driven vortices in the wall jet downstream of the visible flame zone. However, the frequency peaks have smaller magnitudes and wider frequency contribution than those found in Fig. 1b for $\Phi = 4$ and the same Reynolds number and nozzle-plate spacing. Given the smaller RMS magnitudes in Fig. 4a compared to Fig. 1a, the small magnitude of the PSD peaks suggests smaller temperature excursions found in the boundary layer of the premixed flame ($\Phi = 1.0$), producing smaller extremes in the heat flux. The broader frequency contribution to the PSD maximum suggests greater irregularity in the fluctuations of wall heat flux.

3.2. Lifted flame

The radial RMS, PSD, and PDF profiles for a lifted flame with a nozzle Reynolds number of 2800, equivalence ratio of 5.2, and a nozzle-plate spacing of 15 diameters are shown in Fig. 5a–c, respectively. This flame, as shown in the photograph Fig. 5a of Part I, is a lifted, free jet-stabilized flame. The RMS profile in Fig. 5a reveals RMS heat fluxes at the stagnation point of magnitude comparable to the mean. The RMS value changes little with increasing radius until $R = 2$, where it begins to rise. As revealed by the flame structure photos in Part I, the lifted flame at this experimental condition was observed to stabilize in the free jet in a region of apparent distributed, premixed combustion. The associated turbulence and rapid heat release result in large temperature fluctuations at the impingement plate. The corresponding PSD in the stagnation zone reveals large, rapid heat flux fluctuations, with significant frequency content beyond 1300 Hz. This is indicative of the heat release in the free jet and the formation of intense temperature fluctuations in the stagnation zone. The stagnation point PDF in Fig. 5c peaks near zero, but is skewed positive by the upstream mixing of hot products and cool unburned gases.

From $R = 3$ to $R = 5$, the RMS values peak in Fig. 5a, indicating a region in the boundary layer with the widest range of temperature fluctuations. This results from the mixing of hot combustion products and cool unburned gases in the free jet. From $R = 0$ to $R = 6$, the PSD's (Fig. 5b) show a substantial increase in the magnitude, but a slight decrease in contributing frequencies. At the same radial locations, the PDF's in Fig. 5c broaden. The greater temperature ranges in the boundary layer implied by the PSD's and PDF's suggest a region of rapid heat release. Correlating this observation to the flame photograph in Fig. 5a of Part I reveals that the increase in the fluctuation magnitude seen in the RMS and PSD profiles is near the same radial location ($R \approx 6$) as the location of the flame stabilization region in the free jet.

Beyond $R = 6$, the RMS profile of Fig. 5a indicates a gradual, continuous decrease in the heat flux RMS fluctuation range in the wall jet. The corresponding PSD's decrease in magnitude out to $R = 14$. Beyond $R = 14$, the magnitude of the low frequencies increase again. This may be attributed to buoyancy-driven structures discussed previously. These structures are indicated by a 12-Hz preferred frequency that first appears in the PSD's at a radial location eight diameters from the stagnation zone.

Radial heat flux RMS profiles are shown in Fig. 6a for lifted, free jet-stabilized flames at conditions $Re = 2800$, $\Phi = 5.2$, and nozzle-plate spacings of 5, 15, and 25 diameters. All three profiles exhibit a small region of near-constant RMS heat flux extending outward

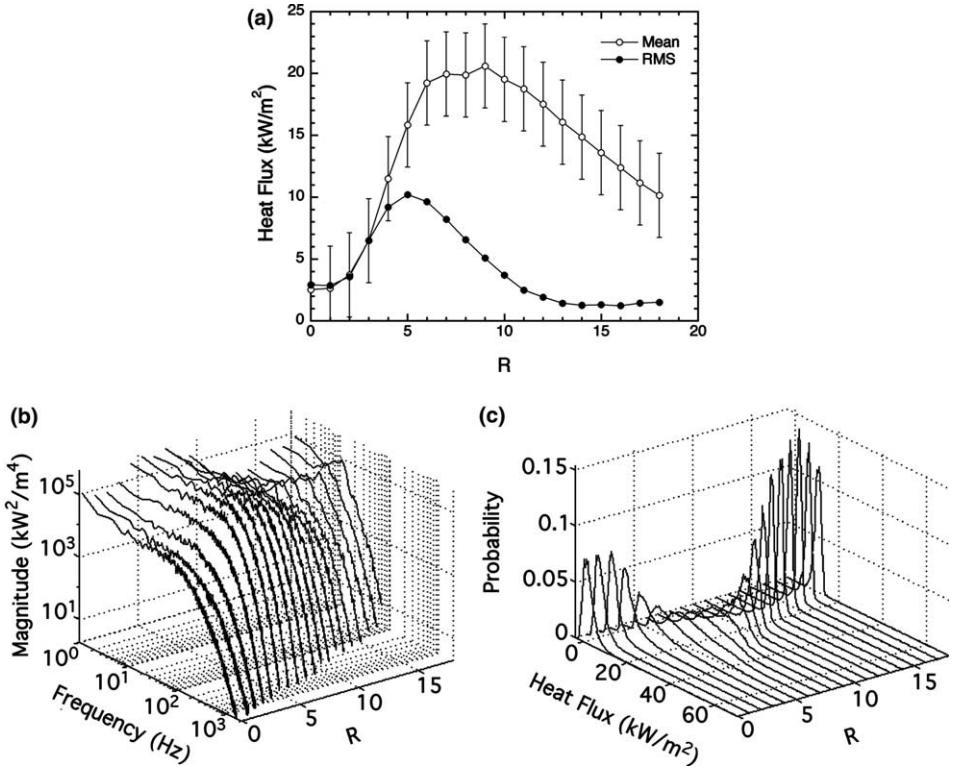

Fig. 5. Heat flux radial variations of (a) mean and RMS; (b) PSD's; and (c) PDF's for a flame with $Re = 2800$, $\Phi = 5.2$, and $H = 15$.

from the stagnation zone. The radial extent of this zone of constant RMS heat flux increases with nozzle-plate spacing, indicative of the growing diameter of the pre-impingement jet with axial distance from the nozzle exit. The RMS heat flux increases with R to a maximum, then decreases for all three nozzle-plate spacings. Similar behavior was observed and explained in the nozzle-stabilized flame characteristics of Fig. 2a.

Fig. 6b and c illustrate the radial heat flux PSD's and PDF's, respectively, for the lifted, free jet-stabilized flame conditions of Fig. 6a ($Re = 2800$ and $\Phi = 5.2$) for a nozzle-plate spacing of 25 diameters. The high RMS values in the stagnation zone are reflected in the magnitude of the PSD's and range of the PDF's, a result of the mixing of the hot combustion products with the cool unburned gases in the free jet. The PSD's for $R > 6$ reveal a weak preferred frequency near 10 Hz, suggesting again the influence of buoyancy- and/or shear-driven vortex structures on the wall jet, as observed in the PSD's of Fig. 5b for the flame at $H = 15$. A comparison of the PSD's for the flames at $H = 15$ (Fig. 5b) and 25 (Fig. 6b) reveals that the range of contributing frequencies in the stagnation zone is smaller at the greater nozzle-plate spacing, but there is a more gradual decrease in the contribution at higher frequencies with R at a nozzle-plate spacing of 25 diameters than at 15 diameters. These differences may suggest larger thermal variations but slower dissipation in the wall jet at higher nozzle-plate spacings.

The changes in the time-resolved stagnation heat flux with equivalence ratio for lifted flames is illustrated by the RMS, PSD, and PDF dependence on Φ shown in Fig. 7a–c for $Re = 2800$ and $H = 15$. Part I describes the transition of flame structure from a stagnation zone-stabilized regime with distributed, premixed combustion throughout most of the flame at $\Phi = 3.0$, to a free jet-stabilized regime with premixed combustion at the flame stabilization point and diffusion-controlled combustion throughout the rest of the flame at $\Phi = 5.0$. This is reflected in the decreasing RMS heat flux illustrated in Fig. 7a from $\Phi = 3.0$ to $\Phi = 5.0$. As the rate of heat release at the flame front decreases with increasing equivalence ratio, the temperature excursions in the flow decrease as well. Therefore, the resulting fluctuations in the heat flux signal decrease, as seen in the decreasing magnitudes of the PSD in Fig. 7b. The PSD's also reveal high magnitudes at higher frequencies for $\Phi = 3.0$, suggesting that the smaller structures of the premixed flames yield larger temperature extremes than those found in diffusion-controlled combustion. The PDF's of Fig. 7c reveal peaked, rather narrow distributions at low Φ, and lower magnitude, broader

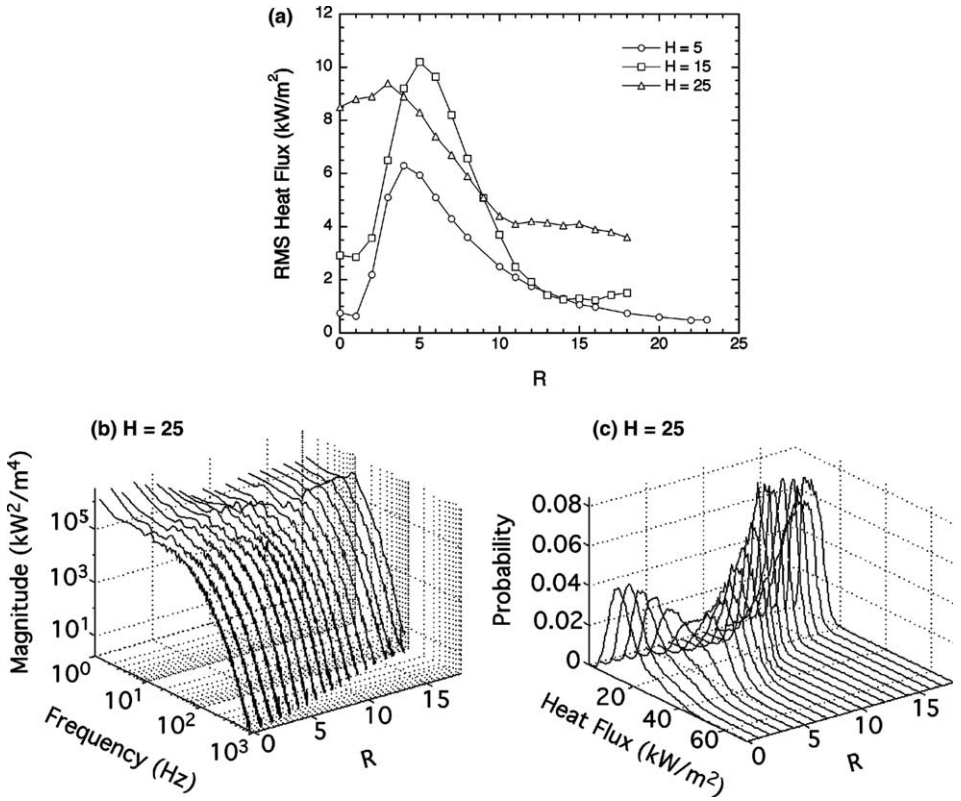

Fig. 6. Heat flux radial variations for a flame with $Re = 2800$, and $\Phi = 5.2$, illustrating (a) the effect of various nozzle-plate spacings on mean and RMS; (b) PSD's and (c) PDF's for $H = 25$.

distributions at higher Φ. For $\Phi > 5.0$, the RMS, PSD, and PDF behavior reveal a gradual increase in the heat flux fluctuation with increasing equivalence ratio. Recall from the discussion of the flame structure in Part I that with increasing equivalence ratio, the flame stabilized closer to the nozzle exit and exhibited more diffusion-controlled combustion. As a result, the length of the flame in the free jet increased, as well as the resulting temperature ranges of the unburned gases within the free jet, resulting in the gradual increase of fluctuation amplitudes of the heat flux seen in Fig. 7a–c.

Fig. 8 illustrates the dependence of time-resolved heat flux on radial position for $Re = 2800$, $H = 15$, and a range of equivalence ratios. Fig. 8a compares the radial RMS heat flux profiles for $\Phi = 3.7$, 5.2, and 8.9. The flame for $\Phi = 3.7$ (corresponding to the flame photograph shown in Part I, Fig. 5d) exhibits significantly higher RMS values than is seen for the two higher equivalence ratios for $R < 6$. As explained in Part I, this is perhaps due to the premixed combustion that occurs in a region near the stagnation zone for increasingly premixed conditions. The higher temperatures associated with premixed combustion and the entrainment of ambient air produce wide fluctuations in heat flux at the impingement plate. The PSD's for this experimental condition at corresponding radial locations shown in Fig. 8b reveal that the magnitude and range of contributing frequencies of the heat flux signal were greater than that of the $\Phi = 5.2$ (and otherwise identical conditions) case shown in Fig. 5b. From the stagnation zone to a radial location of three diameters, the frequency content extends to about 2500 Hz, revealing rapid changes in the heat flux signal. At $R = 4$, the content begins to decrease at higher frequencies with distance from the stagnation zone as the smaller structures produced by the rapid combustion around the stagnation zone begin to dissipate. The corresponding PDF's in Fig. 8c reveal that a weak bimodal distribution develops. At the stagnation point, there is a single peak with a negative heat flux from cool gases impinging the plate. With increasing distance from the stagnation point, a second peak emerges and becomes apparent at $R = 5$. Here, one peak is presumed to be associated with heat transfer from relatively cool gases and a second, higher peak from the hot combustion products. Beyond $R = 5$, the bimodal PDF distribution vanishes, and RMS, PSD's, and PDF's reveal a decrease in the fluctuations that correspond with the relative stability of the wall jet flame. As observed in

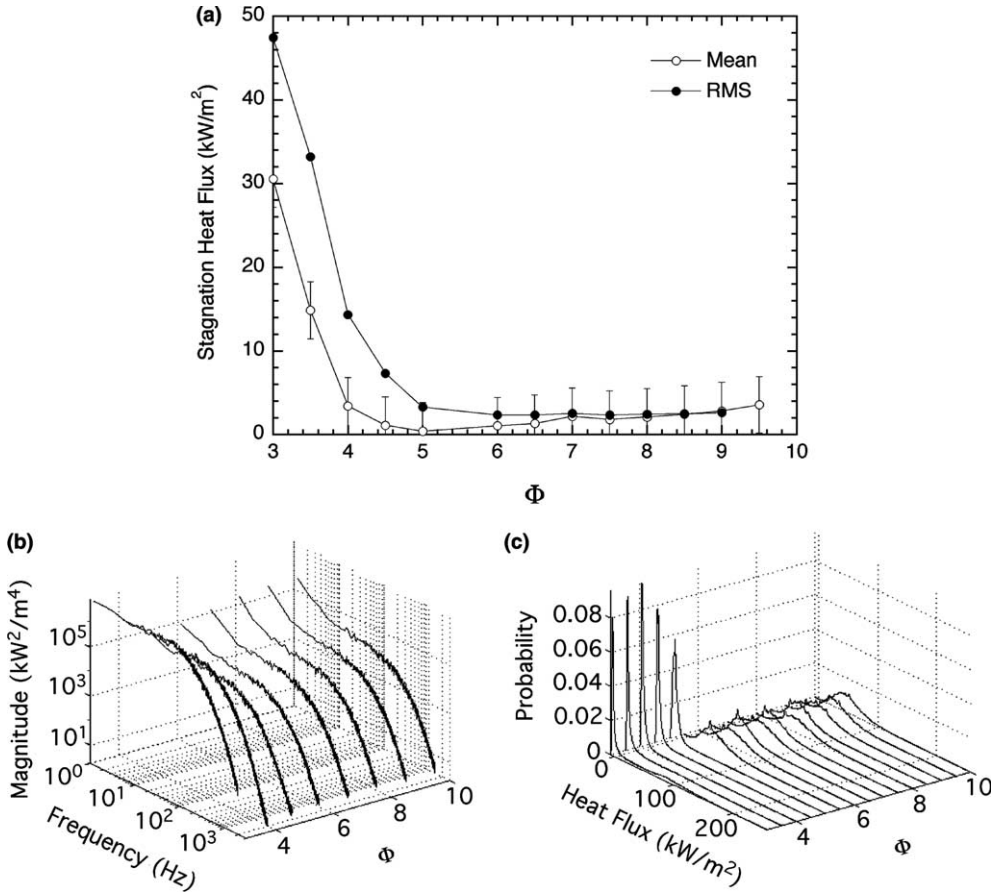

Fig. 7. The effect of equivalence ratio on (a) heat flux mean and RMS; (b) PSD's; and (c) PDF's for a flame with $Re = 2800$ and $H = 15$.

the heat flux PSD's of other wall jet flames, there are weak peaks near 10–20 Hz, again suggesting the formation of buoyancy-driven vortices in the shear layer between the gases surrounding the flame and the ambient air in the free jet.

The RMS, PSD's, and PDF's shown in Fig. 8a, d, and e, respectively, show smaller fluctuations in the wall jet for a flame with $\Phi = 8.9$ ($Re = 2800$, $H = 15$, flame photograph in Fig. 5e of Part I) than those for $\Phi = 5.2$ at otherwise identical conditions (Fig. 5). The RMS measurements along the wall jet boundary layer revealed in Fig. 8a for $\Phi = 8.9$ are slightly smaller at all locations except for $R > 11$. Part I of this investigation revealed that the combustion appears to be diffusion-controlled over the entire surface of the flame for these experimental conditions. This implies slower heat release, resulting in smaller heat flux fluctuations in the wall jet, as seen in the RMS profile. By comparing the magnitudes of the PSD's in Fig. 8d ($\Phi = 8.9$) with those of Fig. 8b ($\Phi = 3.7$) and the ranges of the corresponding PDF's in Fig. 8e with those of Fig. 8c, it may be observed that the heat flux fluctuations are again smaller at higher Φ. There is a reduction in frequency contribution and magnitude at most radial locations along the plate for the richer flame. The PSD's in Fig. 8d again suggest the formation of buoyancy- and/or shear-driven structures in the wall jet by weak preferred frequencies at $R = 12$, but these disappear beyond $R = 22$.

Time-resolved heat flux data for $Re = 5600$ and $\Phi = 5$ are presented in Fig. 9 for nozzle-plate spacings $H = 5$ and 10. A lifted, wall jet-stabilized flame prevailed at these experimental conditions, as illustrated in Part I, Fig. 6. As mentioned in Part I, a flame would not stabilize for $H = 15$ at this Reynolds number and equivalence ratio. Radial profiles of RMS heat flux are shown in Fig. 9a for $H = 5$ and 10, and corresponding PSD's and PDF's for these two nozzle-plate spacings are shown in Fig. 9b–e, respectively. The RMS heat flux in Fig. 9a exhibits near-zero values in the stagnation zone, followed by a rapid rise to a maximum and a subsequent decrease at greater radial locations. The point of peak RMS heat flux corresponds to the point at which the flame was stabilized in the wall jet. This may be explained by random movement of the flame stabilization point, periodically

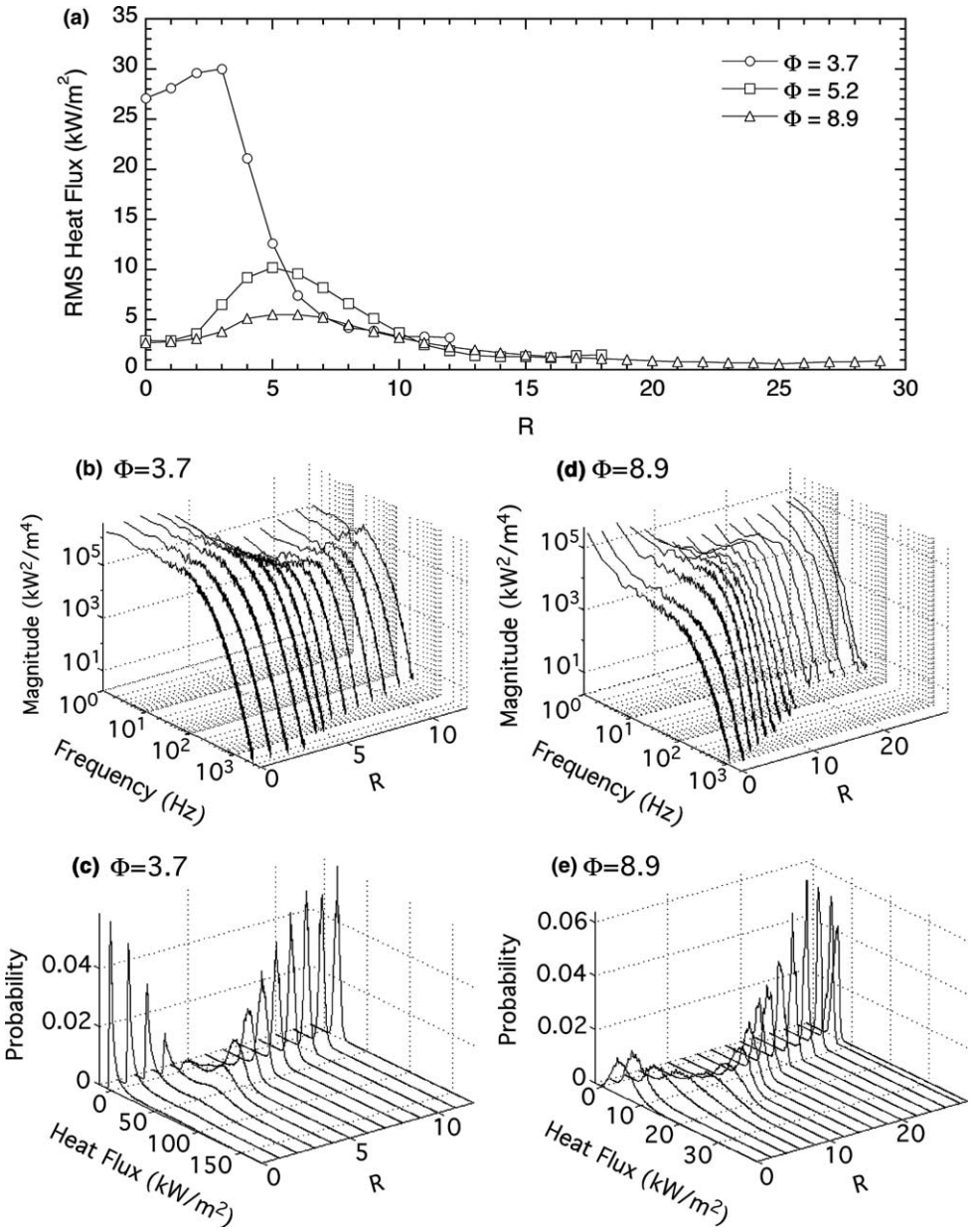

Fig. 8. Radial heat flux profiles for a flame with $Re = 2800$ and $H = 15$, illustrating (a) mean and RMS for various equivalence ratio; (b,d) PSD's; and (c,e) PDF's for $\Phi = 3.7$ and $\Phi = 8.9$.

exposing the plate to hot combustion products and increasing the range of heat fluxes at this location. The corresponding PDF's of Fig. 9c and e are reflective of the radial trends in RMS heat flux shown in Fig. 9a. The fluctuations in heat flux are characterized by peaked, narrow distributions at low R, transitioning to broad distributions at radial locations where the corresponding RMS is high, then a return to narrow peaks at higher R. The broad PDF distributions result from random fluctuation of the flame stabilization within the radial region $4 < R < 12$. PSD's for both nozzle-plate spacings reveal low-magnitude fluctuations with rather broad frequency content for the region $R < 3$ where no flame is seen. Contributing frequencies of the heat flux signal in this radial region extend to 2000 Hz, indicating that the impingement of the cool jet core close to the plate produced very rapid heat flux fluctuations. The broad frequency contribution decreased with radial distance, suggesting dissipa-

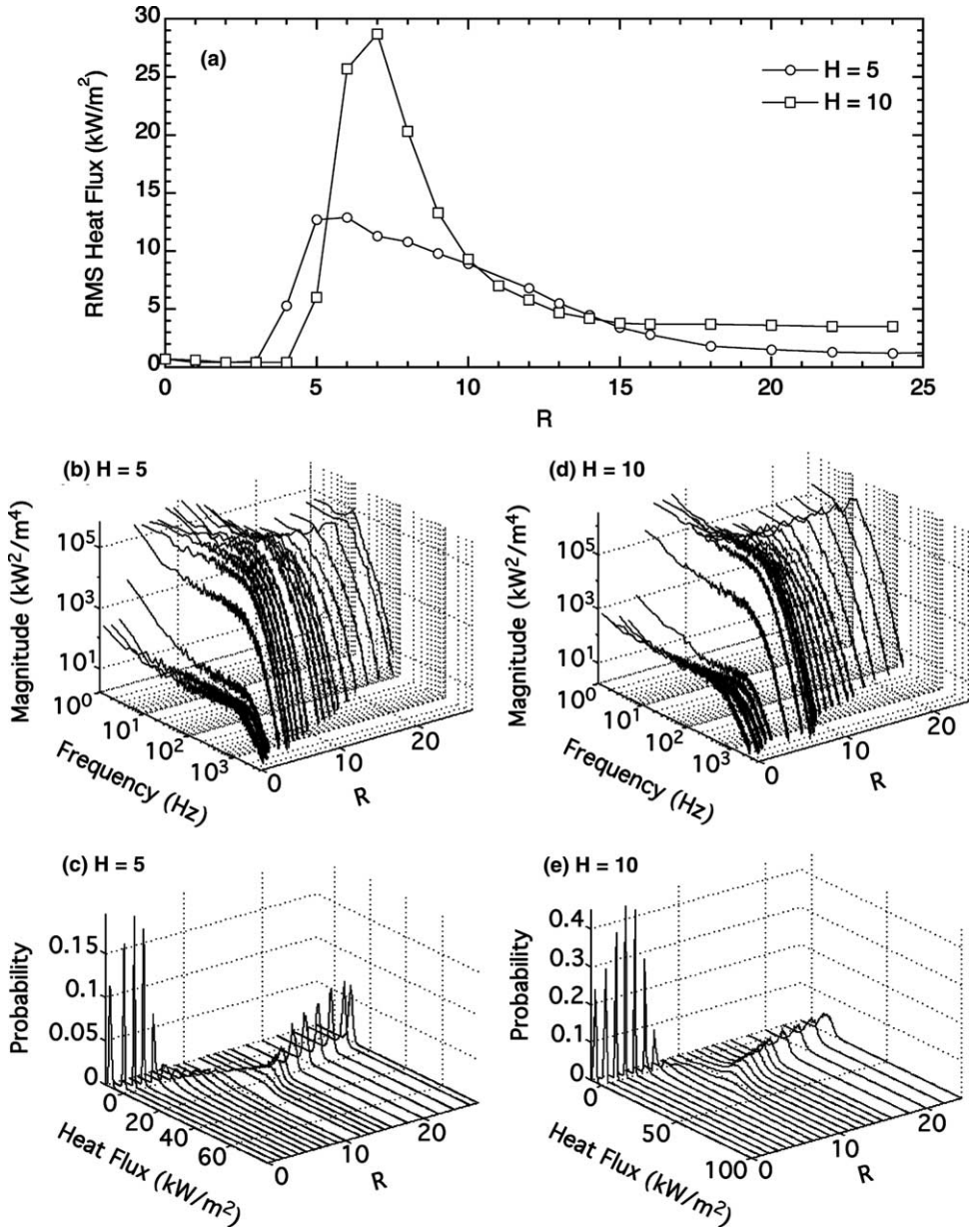

Fig. 9. Radial heat flux profiles for a flame with $Re = 5600$ and $\Phi = 5.2$, illustrating (a) mean and RMS for various two nozzle-plate spacings; (b,d) PSD's; and (c,e) PDF's for $H = 5$ and $H = 10$.

tion of the smaller structures in the flow. A weak but distinguishable preferred frequency at 12 Hz is also observed in the PSD's for both $H = 5$ and 10 beyond $R = 10$, again due to vortex formation in the wall jet. The PDF's for these two nozzle-plate spacings are quite similar, revealing narrow, strongly peaked heat flux distributions early in the wall jet, more broad (bimodal for $H = 10$) distributions for $4 \leqslant R \leqslant 10$, and finally, more narrow distributions for $R > 10$.

3.3. Reynolds number dependence

Following the sequence of discussion in Part I of this work, time-resolved flame impingement heat flux behavior for nozzle-stabilized flame (low-*Re*) and lifted flame (high-*Re*) behavior has been presented in foregoing sections. These two flame structure regimes are now bridged with Fig. 10, in which the RMS, PSD, and PDF's for flames with $\Phi = 7.0$, $H = 15$ are presented

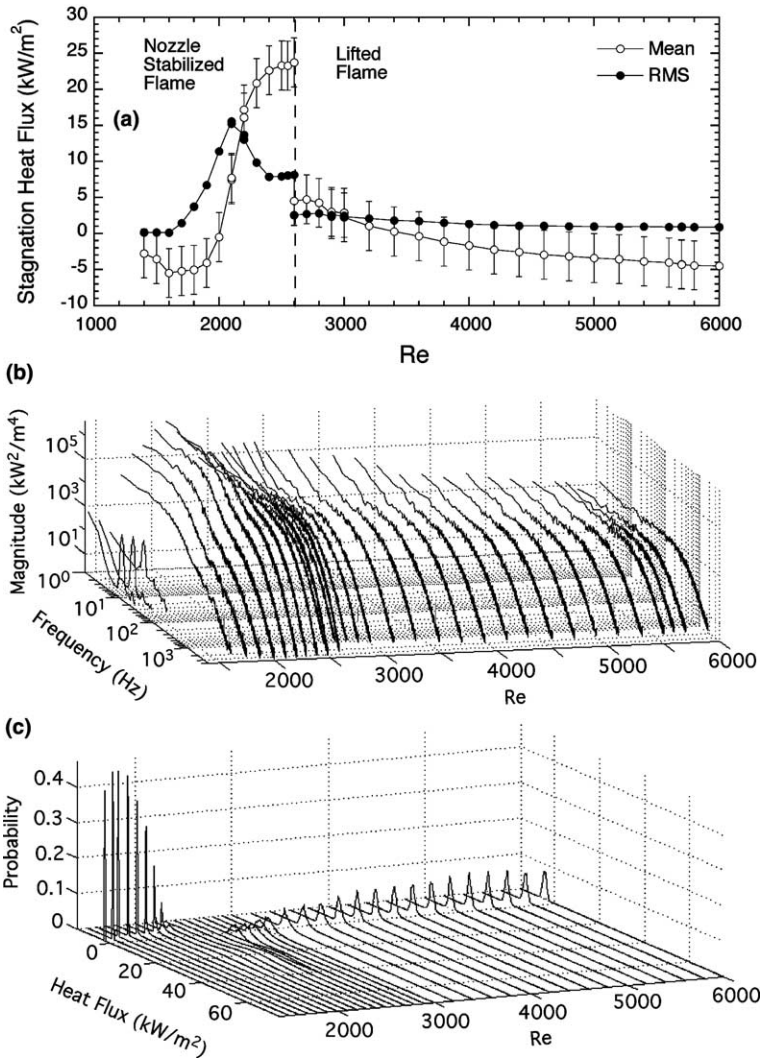

Fig. 10. The effect of Reynolds number on stagnation heat flux: (a) mean and RMS; (b) PSD; and (c) PDF for a flame with $\Phi = 7.0$ and $H = 15$.

for Reynolds numbers between 1400 and 6000. This Reynolds number range spans both nozzle-stabilized and lifted flame regimes. Fig. 10a includes the time-mean heat flux values (which were presented in Part I, Fig. 9c) for comparison. As the Reynolds number is increased, stagnation RMS heat flux magnitudes are observed to rise with an accompanying rise in mean flux, reaching a maximum RMS heat flux near $Re = 2000$. While the mean flux continues to rise with increasing Re, the RMS flux falls to an intermediate value just prior to flame lift-off at $Re = 2600$, the Reynolds number corresponding to transition from nozzle-stabilized to lifted flame combustion. In the lifted flame regime the mean flux decreases gradually while the RMS fluctuations remain nearly independent of Reynolds number. PSD's at low Reynolds number ($Re < 1400$) reveal preferred frequencies characteristic of the buoyancy-induced vortex development in the pre-impingement jet. Such preferred frequencies are not seen at higher Reynolds numbers where jet momentum is dominant. There is significant expansion of contributing frequencies and increase in PSD magnitude as Re is increased above 1600, corresponding to the increase in stagnation RMS heat flux seen in Fig. 10a. As the Reynolds number is further increased the PSD magnitudes also increase, then decrease, until the stabilization regime changes from nozzle-stabilized to lifted flame combustion. Finally, there is gradual decrease in PSD magnitude for Rey-

nolds numbers above 2600. The PDF's in Fig. 10c reveal narrow peaks in heat flux distribution at low Reynolds numbers with negative magnitude, reflective of impingement of cooler gases at the stagnation point. The peaks broaden and decrease in magnitude as Re is increased until $Re = 2000$, where heat fluxes of a wide range of magnitudes contribute to the peak RMS heat flux seen in Fig. 10a. Again, the bimodal distribution seen for $Re = 2100$ may be due to fluctuation of heat fluxes from those characteristic of relatively cool, unburned gases to those of hot combustion products. Once the flame transitions to the lifted regime, the PDF exhibits increasing peak with more narrow heat flux excursions.

4. Conclusions

The time-resolved local heat flux characteristics were measured for impinging methane-air jet flames, with nozzle Reynolds numbers in the range of 1500–6000 (based on nozzle exit conditions), equivalence ratios between 1 and 9, and nozzle-plate spacings varying between 5 and 35 nozzle diameters.

Local time-resolved heat flux measurements at the stagnation point and the boundary layer of the wall jet flame reveal close dependence of the local heat flux on the flame structure. Heat flux from premixed, nozzle-stabilized flames was characterized by small RMS values and frequency behavior indicating the formation of weak, buoyancy-driven vortex structures at the shear layer between the hot gases surrounding the flame and the ambient air. Conversely, diffusion flames were characterized by much larger RMS values and PSD's indicating the development of much larger vortex structures. For some conditions, this yielded bimodal PDF's due to alternating temperatures at the plate surface. Such vortices attenuated and were barely detectable at nozzle-plate spacings less than 10 nozzle diameters. As the Reynolds number was increased past 1600, periodic heat flux oscillations disappeared.

Time-resolved heat flux for lifted flames varied according to flame structure and intensity. PSD magnitudes were related to range of temperatures in the flow; wider temperature ranges produced larger heat flux variations. The frequency contributions were related to the size of the structures in the flow, smaller structures producing faster fluctuations and higher frequency content. The presence of mixing of hot combusting gases with cool products or cooler unburned gases resulted in PDF's that were sometimes bimodal. Regions of diffusion-controlled combustion produce heat flux variations with frequency content characterized by both small magnitudes and narrow frequency content. Small PSD magnitudes corresponded to a peaked PDF from the narrow range of heat flux fluctuations. PSD's of the wall jets for lifted flames again revealed the development of shear-driven vortex development. Finally, PSD's from flames stabilized strictly in the wall jet also showed the development of buoyancy-driven vortex structures, suggesting that their development is not limited to the free jet.

References

[1] C.E. Baukal, B. Gebhart, A review of flame impingement heat transfer studies. Part 2: Measurements, Combust. Sci. Technol. 104 (1995) 359–385.
[2] A.G. Rutherford, I. Fells, Oscillations in aerated Bunsen burner flames, J. Inst. Fuel 42 (1969) 26–28.
[3] D.F.G. Durão, J.H. Whitelaw, Instantaneous velocity and temperature measurements in oscillating flames, Proc. Royal Soc. London, Series A, Math. Phys. Sci. 338 (1974) 479–501.
[4] G.K. Hargrave, M. Fairweather, J.K. Kilham, Forced convective heat transfer from premixed flames. Part 1: Flame structure, Int. J. Heat Fluid Flow 8 (1987) 55–63.
[5] E. Buhr, G. Hapt, H. Kremer, Heat transfer from impinging turbulent jet flames to plane surfaces, in: F.J. Weinberg (Ed.), Combustion Institute European Symposium 1973, Academic Press, New York, 1973, pp. 607–612.
[6] C.D. Donaldson, R.S. Snedecker, D.P. Margolis, A study of free jet turbulent structure and impinging heat transfer, J. Fluid Mech. 45 (1965) 477–512.
[7] M. Fairweather, J.K. Kilham, A. Mohebi-Ashtiani, Stagnation point heat transfer from turbulent methane-air flames, Combust. Sci. Technol. 35 (1984) 225–238.
[8] G.K. Hargrave, M. Fairweather, J.K. Kilham, Turbulence enhancement of stagnation point heat transfer on a body of revolution, Int. J. Heat Fluid Flow 6 (1985) 91–98.
[9] G.K. Hargrave, M. Fairweather, J.K. Kilham, Turbulence enhancement of stagnation point heat transfer on a circular cylinder, Int. J. Heat Fluid Flow 7 (1986) 89–95.
[10] C.J. Hoogendoorn, The effect of turbulence on heat transfer to a stagnation point, Int. J. Heat Mass Transfer 20 (1977) 1333–1338.
[11] C.J. Hoogendoorn, C.O. Popiel, T.H. van der Meer, Turbulent heat transfer on a plane surface in impingement round premixed flame jetsProceedings of the 6th International Heat Transfer Conference—1978, vol. 4, Hemisphere, Washington, DC, 1978, pp. 107–112.
[12] M.E. Horsley, M.R.I. Purvis, A.S. Tariq, Convective heat transfer from laminar and turbulent premixed flamesHeat Transfer—1972, vol. 3, Hemisphere, Washington, DC, 1972, pp. 567–574.
[13] F.C. Lockwood, H.A. Moneib, Fluctuating temperature measurements in turbulent jet diffusion flame, Combust. Flame 47 (1982) 291–314.
[14] G.K. Hargrave, M. Fairweather, J.K. Kilham, Forced convective heat transfer from premixed flames. Part 2: Impingement heat transfer, Int. J. Heat Fluid Flow 8 (1987) 132–138.
[15] R. Matsumoto, T. Nakajima, K. Kimoto, S. Noda, S. Maeda, An experimental study on low frequency oscillations and flame generated turbulence in premixed diffusion flames, Combust. Sci. Technol. 27 (1982) 103–111.

[16] R.S. Figliola, D.E. Beasley, Theory and Design for Mechanical Measurements, second ed., John Wiley & Sons Inc., New York, 1995.
[17] A. Mitra, Fundamentals of Quality Control and Improvement, Prentice-Hall Inc, Upper Saddle River, New Jersey, 1998.
[18] S.G. Tuttle, Characterization of local, time-mean and time-resolved heat transfer from an impinging flame jet, M.S. Thesis, Brigham Young University, 2002, Provo, UT.
[19] A.J. Yule, Large scale structures in the mixing layer of a round jet, J. Fluid Mech. 89 (1978) 413–432.
[20] I. Kimura, Stability of laminar-jet flames, in: 10th Symposium (Int'l) on Combustion, Combustion Institute, Pittsburgh, Pennsylvania, 1965, pp. 1295–1301.
[21] A.J. Yule, N.A. Chigier, S. Ralph, R. Boulderstone, J. Ventura, Combustion-transition interaction in a jet flame, AIAA J. 19 (1981) 752–760.
[22] V.R. Katta, W.M. Roquemore, Role of inner and outer structures in transitional jet diffusion flames, Combust. Flame 92 (1993) 274–282.
[23] M.Q. McQuay, S.M. Cannon, Time-resolved temperature measurements in the developing region of an elliptic, jet diffusion flame at a Reynolds number of 6000, Combust. Sci. Technol. 119 (1996) 13–33.
[24] W.M. Roquemore, L.-D. Chen, L.P. Goss, W.F. Lynn, The structure of jet diffusion flames, in: R. Borghi, S.N.B. Murthy (Eds.), Turbulent Reactive Flows, Lecture Notes in Engineering, 40, Springer-Verlag, Berlin, 1989, pp. 49–88.